Journal of Materials Chemistry A

ROYAL SOCIETY OF CHEMISTRY

PAPER

View Article Online
View Journal | View Issue

Cite this: J. Mater. Chem. A, 2024, 12, 31276

Reversible K-ion intercalation in $CrSe_2$ cathodes for potassium-ion batteries: combined *operando* PXRD and DFT studies†

Weihao Li, [a] Johannes Döhn,[b] Jinyu Chen,[cd] Manuel Dillenz, [b] Mohsen Sotoudeh, [b] David M. Pickup,[e] Shunrui Luo, [f] Ryan Parmenter,[e] Jordi Arbiol, [fg] Maria Alfredsson, [e] Alan V. Chadwick,[e] Axel Groß, [bh] Maider Zarrabeitia *[cd] and Alexey Y. Ganin *[a]

In the pursuit of more affordable battery technologies, potassium-ion batteries (KIBs) have emerged as a promising alternative to lithium-ion systems, owing to the abundance and wide distribution of potassium resources. While chalcogenides are uncommon as intercalation cathodes in KIBs, this study's electrochemical tests on $CrSe_2$ revealed a reversible K^+ intercalation/deintercalation process. The $CrSe_2$ cathode achieved a KIB battery capacity of 125 mA h g^{-1} at a 0.1C rate within a practical 1–3.5 V *vs.* K^+/K operation range, nearly matching the theoretical capacity of 127.7 mA h g^{-1}. Notably, the battery retained 85% of its initial capacity at a high 1C rate, suggesting that $CrSe_2$ is competitive for high-power applications with many current state-of-the-art cathodes. *In-operando* PXRD studies uncovered the nature of the intercalation behavior, revealing an initial biphasic region followed by a solid-solution formation during the potassium intercalation process. DFT calculations helped with the possible assignment of intermediate phase structures across the entire $CrSe_2$–$K_{1.0}CrSe_2$ composition range, providing insights into the experimentally observed phase transformations. The results of this work underscore $CrSe_2$'s potential as a high-performance cathode material for KIBs, offering valuable insights into the intercalation mechanisms of layered transition metal chalcogenides and paving the way for future advancements in optimizing KIB cathodes.

Received 23rd July 2024
Accepted 21st October 2024

DOI: 10.1039/d4ta05114a

rsc.li/materials-a

Introduction

The surge in global demand for portable electronics and electric vehicles has intensified the need for cost-effective, environmentally friendly battery solutions.[1–3] Potassium-ion batteries (KIBs) have emerged as a compelling alternative to traditional lithium-ion systems, leveraging the abundance and wide distribution of potassium resources across the globe.[4–6] KIBs offer several advantages over their lithium-ion counterparts. Notably, the K^+ has an even smaller Stokes radius than Li^+, enabling rapid diffusion in common electrolytes, such as propylene carbonate.[7,8] This property leads to superior rate capabilities in KIBs compared to lithium-ion batteries (LIBs). Additionally, the larger K-ion radius allows it to remain within interstitial sites, preventing long-term degradation commonly observed in LIBs where small Li ions often substitute transition metals within the lattice.[9] Furthermore, since potassium does not form alloys with Al, cheaper and lighter Al-foils can be routinely used as current collectors in KIBs.[10]

Despite significant progress in KIB research over the past decade, the field remains in its nascent stages compared to the more established LIBs. Key efforts have been focused on metal oxide-based cathodes,[11] with optimization processes such as doping[12] aimed at achieving performance comparable to LIBs. Prussian blue analogues with 3D frameworks[13–17] have also garnered attention, particularly where safety is a concern. However, challenges, such as volume changes,[14] low density,[15] and poor electronic conductivity resulting in low coulombic efficiency (CE)[18] still need to be addressed.

In this context, metallic and semiconducting layered transition metal chalcogenides (TMCs) offer promising systems for KIB cathode development. Compared to oxides, TMCs display

[a]School of Chemistry, University of Glasgow, G12 8QQ, Glasgow, UK. E-mail: Alexey.Ganin@glasgow.ac.uk
[b]Institute of Theoretical Chemistry, Ulm University, 89081, Ulm, Germany
[c]Helmholtz Institute Ulm (HIU), Helmholtzstrasse 11, 89081, Ulm, Germany. E-mail: maider.ipina@kit.edu
[d]Karlsruhe Institute of Technology (KIT), P.O. Box 3640, D-76021 Karlsruhe, Germany
[e]School of Physical Sciences, University of Kent, CT2 7NH, Canterbury, Kent, UK
[f]Catalan Institute of Nanoscience and Nanotechnology (ICN2), CSIC and BIST, Campus UAB, Bellaterra, 08193, Barcelona, Catalonia, Spain
[g]ICREA, Pg. Lluís Companys 23, 08010 Barcelona, Catalonia, Spain
[h]Helmholtz Institute Ulm (HIU) for Electrochemical Energy Storage, 89081, Ulm, Germany

† Electronic supplementary information (ESI) available. See DOI: https://doi.org/10.1039/d4ta05114a

wider interlayer spacing, making them attractive hosts for the relatively large K^+. While many binary TMCs studied to date demonstrate conversion-type reactions leading to complete degradation of the host material,[19,20] notable exceptions like TiS_2 (ref. 21) and $KCrS_2$ (ref. 22) have shown promising reversible intercalation behavior. In particular, the $KCrS_2$ system has demonstrated the ability to cycle repeatedly between $\sim K_{0.4}CrS_2$ and $\sim K_{0.8}CrS_2$ without side reactions. However, due to such a small intercalation range, the battery showed a relatively low capacity of only ~68 mA h g^{-1} at a very slow rate of 0.05C.

This is significantly lower than the expected theoretical capacity of ~231 mA h g^{-1}. To address these limitations, increasing the polarizability of the anion could alleviate drastic phase transitions and improve the extent of the intercalation reaction during charge–discharge cycles. This suggests that replacing S with Se could lead to improved KIB performance. Remarkably, $CrSe_2$ has not been studied in KIBs to date despite being demonstrated to readily intercalate K^+ to $KCrSe_2$.[23–25] Therefore, this work used the excellent opportunity to investigate whether the K^+ intercalation process in $CrSe_2$ can be pushed to its theoretical limit while delivering competitively high battery performance along the way.

Results and discussion

To understand intercalation process of K^+ into $CrSe_2$, we carried out periodic density functional theory (DFT) calcualtions which are shown to yield reliable information about batteries.[26] In particular, we have determined the density of states (DOS) to elucidate the electronic structures of $CrSe_2$ and $KCrSe_2$. Furthermore, we have performed a computational screening study[27,28] to identify the crystal structure as a function of K loading. The geometries of $CrSe_2$ and $KCrSe_2$ in the respective space groups $P\bar{3}m1$ and $C2/m$ were optimized with the strongly constrained and appropriately normed (SCAN) meta-generalized gradient approximation,[29] and the DOS were calculated with the hybrid functional suggested by Heyd, Scuseria, and Ernzerhof (HSE06)[30] as described in ESI Note 1.† The partial DOS for each compound (Fig. 1) and the contribution of the relevant bands are in line with previous computational studies.[25,31,32]

In both materials, the filled valence band, which starts at about −6 eV, is in the spin-up direction predominantly of Cr(d) character but exhibits significant Se contributions, suggesting a partially covalent nature of the bonding as found for other layered materials.[33,34] Interestingly, the lowest unoccupied states of $CrSe_2$ and the highest occupied states of $KCrSe_2$ are dominated by Se in both spin states. Hence, in contrast to other layered cathode materials like $LiCoO_2$, where the redox reaction is driven by oxidation/reduction of the transition metal,[26,35,36] the present observations indicate anionic contributions to the redox process in $KCrSe_2$. Notably, there are no contributions of K to the valence band of $KCrSe_2$, confirming the full ionization to K^+ during intercalation. We noted metallic behavior in the case of $CrSe_2$, while $KCrSe_2$ is a semiconductor with a band gap of 1.57 eV, suggesting that the electronic conductivity of the intercalated material is impaired compared to the pristine material.

The DFT calculations point out that due to the semiconducting behavior of $KCrSe_2$, a KIB based on $CrSe_2$ would benefit from conductive additives. Therefore, we designed an efficient synthesis which allows for the direct addition of graphite to $CrSe_2$ without affecting the materials' properties, as discussed at length elsewhere[25] and ESI Note 1.† The oxidation states of the elements in pristine $CrSe_2$ and $CrSe_2$ with an optimal addition of 10 wt% of graphite are identical, as evidenced by a perfect overlap of the Cr K-edge XANES profiles (Fig. 2a).

A +6.45 eV shift of the Cr-edge relative to that of Cr foil is close to the shift of +5.79 eV measured in the four valent chromium metal in $CrSe_3$.[37] This seems to confirm the valence state of Cr to be +4. Similarly, the analysis of Se K-edge XANES spectra (Fig. S1†) confirmed the same Se oxidation state for both samples. Bond lengths and fitting parameters from EXAFS data are summarized in Tables S1 and S2.† In both $CrSe_2$ samples, the length of the Cr–Se bond is 2.47 Å. Overall, the results are in good agreement with the literature,[38] confirming that the addition of graphite for improved conductivity does not change the chemical identity of $CrSe_2$.

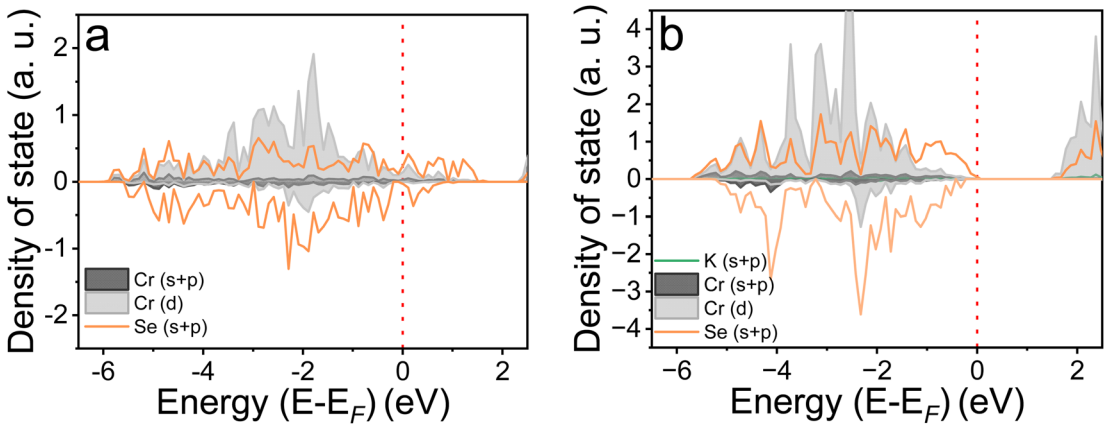

Fig. 1 The partial density of states of the valence bands of (a) $CrSe_2$ and (b) $KCrSe_2$. The Fermi energy E_F is given by a dashed line.

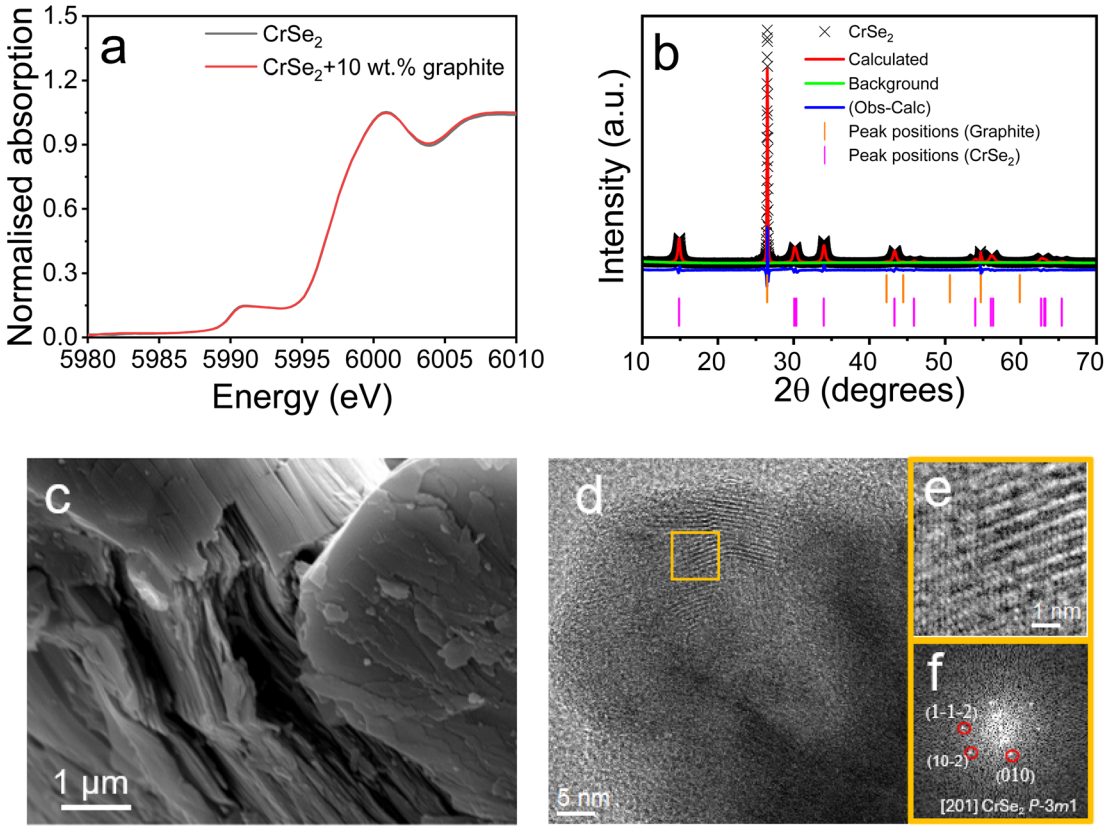

Fig. 2 (a) Cr K-edge XANES profile of pure $CrSe_2$ (black) and $CrSe_2$ with 10 wt% of graphite (red). (b) LeBail refinement of the experimental PXRD profile (CuK_α) for a $CrSe_2$ with 10 wt% of graphite against relevant structure models for $CrSe_2$ and graphite. Experimental data are shown as black crosses; the calculated profile is shown by a solid red line. The difference between the calculated and experimental data is shown as a blue profile. Magenta and orange vertical bars represent the Bragg positions of the $CrSe_2$ and graphite phases. (c) SEM image of $CrSe_2$ with 10 wt% of graphite. (d) HRTEM image of $CrSe_2$ with 10 wt% of graphite. (e) HRTEM magnified detail of the yellow squared region in (d) showing the $CrSe_2$ crystalline structure. (f) Power spectra (Fourier Transform) applied to (e), with the corresponding crystal structure indexing.

The powder X-ray diffraction (PXRD) analysis (Fig. 2b) confirmed that the sample consists of pure $CrSe_2$ and graphite phases without any additional impurities. This is in line with expectations since the precursor consisted of only $KCrSe_2$ and graphite phases (Fig. S2†). The LeBail refinement (carried out instead of the Rietveld refinement due to strong preferred orientation within the sample) of the PXRD data (Fig. 2b) against a model for $CrSe_2$ (Space group (SG): $P\bar{3}m1$) and graphite (SG: $P6_3mc$) showed an excellent match between the experimental data and the calculated profiles, further confirming that the sample contains only two phases. The refined unit cell parameters ($a = 3.3886(3)$ Å, $c = 5.9172(3)$ Å for $CrSe_2$ and $a = 2.4610(8)$ Å, $c = 6.6950(1)$ Å for graphite) are consistent with those in the literature (Table S3†) further confirming that the addition of graphite does not affect the crystal structure of $CrSe_2$. Since the characterization by EXAFS and PXRD showed that the pristine $CrSe_2$ and $CrSe_2$ with 10 wt% of graphite samples are chemically equivalent, from this point, we refer to the graphite-containing samples simply as $CrSe_2$ since only these were used in the cell testing work.

The SEM revealed a lamellar morphology of the sample (Fig. 2c and S3†), while the elemental mapping by EDX revealed perfectly overlapped Cr and Se maps (Fig. S4†), confirming homogenous $CrSe_2$ phase distributed within the graphite matrix. HRTEM revealed that the sample is highly crystalline (Fig. S5†). From the crystalline domain in Fig. 2d, the $CrSe_2$ lattice fringe distances were measured to be 2.108 Å, 2.051 Å, and 2.867 Å, while the angles between the first and the next measured spots corresponded to 39.15° and 109.6°, respectively. With the former structural information, we could index the power spectrum (Fourier Transform) and assign the found crystal structure to the trigonal $CrSe_2$ phase, as visualized along its [201] zone axis. Furthermore, the simulations revealed that the crystal structure of the studied region is fully consistent with the one expected for $CrSe_2$ (SG: $P\bar{3}m1$ with $a = 3.3931$ Å and $c = 5.9150$ Å), which matched well with the PXRD results. Furthermore, the individual EDX maps of Cr and Se are perfectly overlapped further confirming the homogeneity of the sample on a nearly atomic level (Fig. S5†).

The electrochemical measurements were carried out using $CrSe_2$ as a cathode and K metal as an anode with 1 M KPF_6 in EC : DMC as an electrolyte (ESI Note 1† for details). The cyclic voltammetry (CV) measurements at 0.1 mV s^{-1} (Fig. 3a) revealed several peaks, pointing to a complex intercalation behavior. However, a near-perfect overlap of the profiles on the first and second discharge/charge clearly suggests a reversible

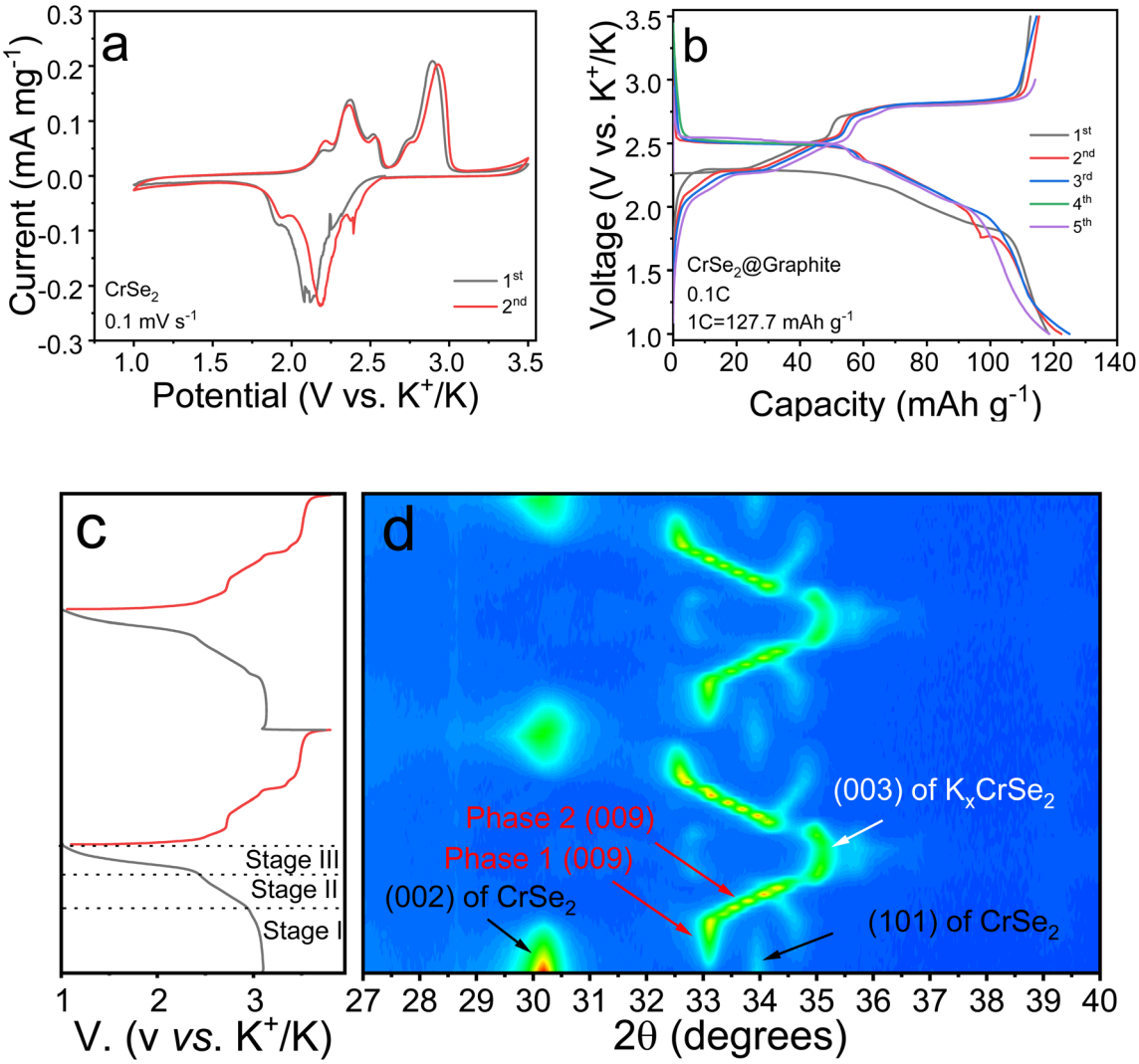

Fig. 3 (a) CV profiles of $CrSe_2$ recorded at 0.1 mV s^{-1}, (b) GCD profiles of $CrSe_2$ recorded at 0.1C scan rate at 20 °C ± 2 °C. (c) GCD profiles of $CrSe_2$ and (d) corresponding contour plot of *in operando* PXRD data. The Miller indexes of key reflections of the expected phases are provided within the figure.

intercalation/deintercalation process without any evidence of blockages or decomposition of $CrSe_2$.

Galvanostatic charge/discharge (GCD) profiles (Fig. 3b) at a relatively low charge/discharge rate of 0.1C (corresponding to 12.77 mA g^{-1}) further confirmed the intercalation of K^+ into $CrSe_2$.

The cell delivered a capacity of 125 mA h g^{-1} on the second discharge, which is very close to the theoretical capacity of 127.7 mA h g^{-1}. In this regard, $CrSe_2$ outperforms a range of state-of-the-art cathodes for KIBs reported up to date (Table S4†).[22,39–41] Notably, the shapes of the GCD profiles are markedly different from those observed for the $KCrS_2$ battery, which was only partially reversible and, as a result, delivered only 68 mA h g^{-1} at a 0.05C.[22]

Additional tests were conducted on pure graphite, which demonstrated negligible capacity contribution of less than 1.4 mA g^{-1} within the 1.0–3.5 V potential range (Fig. S7†). The comprehensive study for choosing 10 wt% as the optimal ratio is discussed at length elsewhere.[25] The details of the sample preparation are summarized in ESI Note 1.†

Furthermore, following the approach discussed at length in the previous study,[42] we calculated (ESI Note 1, Fig. S8 and S9†) the values of the apparent diffusion coefficients $D_{C1} = 7.3 \times 10^{-11}$ cm^2 s^{-1} (for the deintercalation from Stage 3 to Stage 2) and $D_{C2} = 3.8 \times 10^{-11}$ cm^2 s^{-1} (for the deintercalation from Stage 2 to Stage 1) were higher than in $KCrS_2$ (6×10^{-12} cm^2 s^{-1}).[22] These values were of the same order of magnitude as state-of-the-art Prussian blue cathodes ($5 \times 10^{-4} \times 10^{-10}$ cm^2 s^{-1}),[43] suggesting that $KCrSe_2$ is a promising K-based cathode material.

The results from the rate capacity experiments upon cycling at various C-rates (Fig. S10†) showed that the battery retained 85% of the initial capacity even when cycled at a relatively high 1C rate, showing promising electrochemical behaviour for high-power applications. Moreover, the battery retained 80% of the initial capacity after 70 cycles investigated in a galvanostatic

mode at a 0.1C rate (Fig. S11†). This is similar to previously reported layered cathode materials (Table S4†). However, upon further cycling the cell exhibited capacity fading (Fig. S11†). To understand this issue, a comprehensive assessment of electrolytes commonly used in KIB research was conducted, revealing that none outperformed the 1 M KPF_6 in 1 : 1 EC : DMC electrolyte (Fig. S12†). The significant impact of electrolyte composition on battery performance strongly suggests that further optimization could lead to improved cycling stability. Previous studies have reported on the detrimental effects of electrolyte instability on cycling performance, particularly due to erosion of the solid-electrolyte interphase.[44] Recent strategies to mitigate this issue include the use of sacrificial agents such as $K_2C_4O_4$.[45]

In addition, the coulombic efficiency (CE) value of 97% is delivered, which is gradually trending down until reaching the minimum of *ca.* 95% on cycle 50. Nevertheless, in the following cycles the CE is gradually improved to almost reach 100% (see Fig. S11†). These CE values are in the range of the commonly observed in KIBs, *e.g.*, between 94 and 98%.[46,47]

Future work aimed at optimization of the electrolyte composition may help to solve the issue of capacity fading upon cycling and goes beyond the scope of this preliminary investigation. Additionally, solvothermal synthesis that has the potential to produce hierarchical compounds could lead to optimization,[48,49] which can improve both the performance and scalability of cathode material production.[50]

Since $CrSe_2$ has not been previously reported as a battery cathode, it is essential to understand the intercalation processes that drive battery performance in this material. Therefore, *in-operando* PXRD datasets were recorded on $CrSe_2$ alongside the experimentally measured GCD profiles at a 0.2C rate (Fig. 3c). The extent of K^+ ion intercalation as the value of x in K_xCrSe_2 can be evaluated from a comparison between experimental and theoretical capacity (Fig. S13†). This leads to several stages corresponding to different phase assemblies. During the initial **Stage I** the (101) peaks in $CrSe_2$ are visible but of significantly less intensity than expected from a theoretical pattern. It is evident that the $CrSe_2$ has a strong (00l) preferential orientation, as evident from the excess in the intensity of the (002) peaks (Fig. 3c). As intercalation progresses, the formation of the plateau in the electrochemical data is accompanied by the gradual disappearance of the (002) peak from $CrSe_2$ and the appearance of new peaks at ~33° of 2Theta consistent with **Phase 1**, suggesting a biphasic reaction, and corresponding to a ~$K_{0.5}CrSe_2$ composition from the electrochemical data (Fig. S13†). The identity of **Phase 1** is discussed later in the text as it required DFT calculations to identify its probable crystal structure. Upon further charging to **Stage II**, coinciding with a change in the gradient of the curve at ~2.3 V *vs.* K^+/K, the peaks at ~33° 2Theta degrees diverge toward higher 2Theta values from the initial position, suggesting that unknown solid-solutions, such as $K_{0.5+x}CrSe_2$ (denoted as **Phase 2**), is formed. **Phase 2**, with its crystal structure later assigned by DFT, is retained until the voltage reaches ~2 V *vs.* K^+/K, corresponding to a ~$K_{0.8}CrSe_2$ composition according to the electrochemical data (Fig. S13†). Below this voltage, **Phase 3** is retained (consistent with the change in the gradient of the discharge curve slope indicated as **Stage III**) until the maximum capacity consistent with the composition $K_{1.0}CrSe_2$ is achieved. Despite a significantly preferred orientation within the sample with only (003) peaks of appreciable intensity, we could match the boundaries **Phase 3** and the *c*-parameter with the previously reported $K_{0.8}CrSe_2$ and $K_{1.0}CrSe_2$ compositions.[23] The same behavior is observed on discharge as well as the additional charge–discharge cycle (Fig. 3d), confirming the reversibility of the K^+ storage mechanism.

As mentioned above, to identify the possible crystal structures of **Phase 1** and **Phase 2**, we needed to perform periodic DFT calculations for the crystal structures within the entire range of K_xCrSe_2 (x = 0–1). To create potential configurations, we used supercells with 24 to 48 atoms, which were generated by introducing interstitials and vacancies into the crystal structures of $CrSe_2$ (SG: $P\bar{3}m1$) and $KCrSe_2$ (SG: $C2/m$). Additionally, we considered the prototype phase consistent with the structure of $NaCrSe_2$ (SG: $R\bar{3}m$).[23,32] After having removed symmetrically equivalent geometries, we considered 75 input structures in space group $P\bar{3}m1$, 130 input structures in space group $C2/m$, and 55 input structures in space group $R\bar{3}m$. A DFT geometry optimization with the functional suggested by Perdew, Burke, and Ernzerhof (PBE) was conducted on these input structures as described in ESI Note 1,† and the formation energies for the one-dimensional chemical space K_xCrSe_2 (x = 0–1) are plotted in Fig. 4a.

The convex hull of stability has been determined and is highlighted in Fig. 4. In agreement with the experimental observations described above, the calculations revealed that energetically favorable configurations for $K_{0.5}CrSe_2$ are consistent with the monoclinic unit cell (SG: $C2/m$), while for $K_{0.25}CrSe_2$ the most stable structure was found within $P\bar{3}m1$ space group. The diffraction patterns of the most stable phases calculated with the PBE functional are shown in Fig. S14.†

To reassess these computational results, we additionally performed geometry optimizations with the advanced SCAN functional on a set of 52 vacancy structures, which had turned out to be energetically most favorable in the previously conducted PBE calculations (See ESI Note 1† for more details). The *meta*-GGA SCAN has been found to yield significantly improved formation energies compared to generalized gradient approximation-based functionals[51] and is, therefore, expected to provide more reliable results than PBE on the cost of higher computational effort.

The formation energies for this second set of calculations are plotted in Fig. 4b. The calculations revealed only one stable structure with a monoclinic symmetry for $K_{0.5}CrSe_2$ with the simulated structure displayed in Fig. S15.† As mentioned above, despite significant preferred orientation, it appears that the (009) peak of this stable structure fits very well with the peak at ~33.3° of 2Theta from the *in-operando* data (Fig. 3c) while the (-206) and (20-6) peaks could be potentially attributed to experimental peaks at ~34.5° of 2Theta. Based on this assessment, once $CrSe_2$ is completely transformed into $K_{0.5}CrSe_2$, additional K^+ ion intercalation results in the formation of a series of solid-solutions accompanied by a gradual decrease in (009) peak. This decrease is consistent with the plot of the *c*-

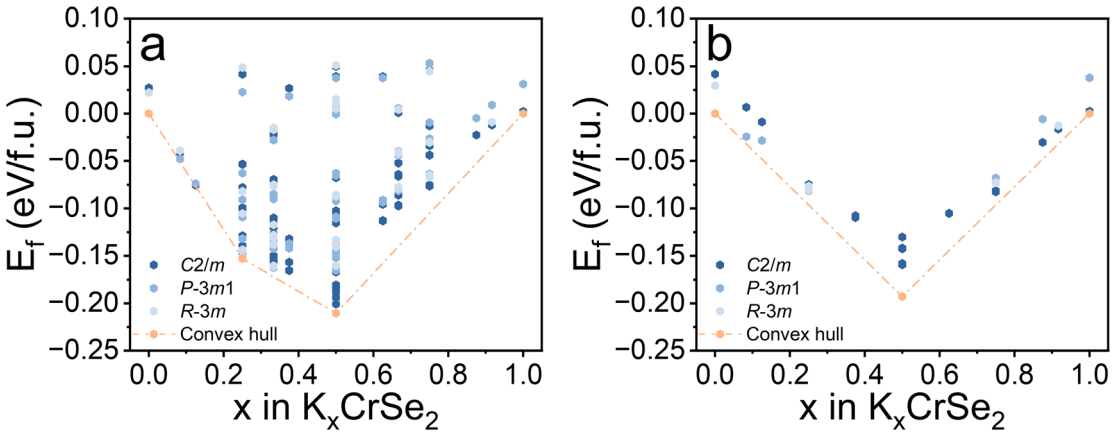

Fig. 4 Formation energies E_f of the one-dimensional phase space K_xCrSe_2 ($0 \leq x \leq 1$) evaluated with (a) the PBE functional and (b) the SCAN functional. The compounds on the convex hull of stability are highlighted in red.

parameters for the DFT-deducted phases along the energy hull (Fig. S16†). Notably, DFT calculations predict that these phases are metastable. Therefore, it is unsurprising that previous researchers were unable to detect them (Table S6†) in *ex situ* experiments.[23] Despite possible metastability, it appears that all the K^+ ion intercalated phases remain intact during the cycling process. As mentioned above, the significantly preferred orientation of the sample with respect to the plane did not allow for complete indexing of **Phase 1** and **Phase 2**. This, however, provides an opportunity for future follow-up work, given the relatively good performance of the $CrSe_2$ battery.

Conclusion

In summary, $CrSe_2$ emerges as a promising cathode material for KIBs, achieving a capacity of 125 mA h g^{-1} at 0.1C rate, nearly matching its theoretical capacity. *In-operando* PXRD studies and DFT calculations reveal three distinct phases during K^+ intercalation, providing crucial insights into the potassiation process, such as an initial biphasic region followed by a solid-solution one. $CrSe_2$ exhibits reversible intercalation/deintercalation and outperforms its sulfur counterpart, $KCrS_2$. While these results are encouraging, challenges persist, including the need to enhance long-term cycling stability and fully comprehend structural changes during intercalation. Future research should prioritize electrolyte composition optimization, investigation of intermediate phase structures, and exploration of doping effects to improve the electronic conductivity of the fully intercalated semiconducting $K_{1.0}CrSe_2$ phase. Despite these hurdles, this work significantly advances the development of efficient and sustainable energy storage solutions. It demonstrates that research into TMC-based cathodes for KIBs could create substantial impact on the pursuit of alternatives to LIBs, paving the way for more sustainable energy storage technologies.

Data availability

All electronic structure calculations used in this work are made available under the Creative Commons Attribution license (CC BY 4.0) on the NOMAD repository (**https://nomad-lab.eu**) within the dataset "CrSe2_as_battery_cathode", **https://dx.doi.org/10.17172/NOMAD/2024.07.18-1**.

Author contributions

A. Y. G. and W. L designed the synthetic work. A. G., J. D., M. D., and M. S. designed, analysed, and interpreted the results of the DFT work. W. L. carried out the synthesis, characterization and processing of the experimental data. D. M. P., R. P., M. A., and A. V. C. collected, processed and interpreted XAS data with the help of W. L. S. L. and J. A. carried out measurements and interpreted TEM data. J. C. and M. Z designed the experiments, carried out and processed electrochemical data and *in-operando* PXRD with the help of W. L. and A. Y. G. The team was managed by A. Y. G. All authors contributed to writing the manuscript and have granted their approval for the final version.

Conflicts of interest

The authors declare no conflict of interests.

Acknowledgements

We acknowledge the financial support by China Scholarship Council, Jim Gatheral Scholarship and mobility funding from the University of Glasgow. A. Y. G acknowledges EPSRC (EP/W03333X/1) for supporting this work. J. C. and M. Z. also acknowledge Bundesministerium fur Bildung und Forschung (BMBF) with the project "SPIRIT", supported by M-ERA.net (03X90508). Support by the German Research Foundation (DFG) under Germany's Excellence Strategy – EXC 2154 – Project number 390874152 (POLiS Cluster of Excellence) is gratefully acknowledged. Computational resources have been provided by the state of Baden-Wuerttemberg through bwHPC and the German Research Foundation (DFG) through Grant No. INST 40/575-1 FUGG (JUSTUS 2 cluster). This work contributes to the research performed at CELEST (Center for Electrochemical Energy Storage Ulm-Karlsruhe). ICN2 acknowledges funding

from Generalitat de Catalunya 2021SGR00457. This study is part of the Advanced Materials programme and was supported by MCIN with funding from European Union NextGenerationEU (PRTR-C17. I1) and by Generalitat de Catalunya. ICN2 is supported by the Severo Ochoa program from Spanish MCIN/AEI (Grant No. CEX2021-001214-S) and is funded by the CERCA Programme/Generalitat de Catalunya. ICN2 is founding member of e-DREAM. We thank the Diamond Light Source for the award of beam time as part of the Energy Materials Block Allocation Group SP31218.

Notes and references

1 R. Mu, G. Suo, C. Lin, J. Li, X. Hou, X. Ye, Y. Yang and L. Zhang, *J. Colloid Interface Sci.*, 2024, **671**, 601–610.
2 G. Suo, Y. Cheng, R. Mu, X. Hou, Y. Yang, X. Ye and L. Zhang, *J. Colloid Interface Sci.*, 2023, **641**, 981–989.
3 Y. Wang, K. Helmbrecht, W. Li, M. Dillenz, Y. Wang, A. Groß and A. Y. Ganin, *ACS Appl. Mater. Interfaces*, 2024, **16**, 50671–50678.
4 T. Hosaka, K. Kubota, A. S. Hameed and S. Komaba, *Chem. Rev.*, 2020, **120**, 6358–6466.
5 Z. Maider, C.-G. Javier, L. Michal, A. Henry, I. Boyan, J. S. S. Thomas, P. Stefano and C.-M. Elizabeth, *Energy Mater.*, 2023, **3**, 300046.
6 Y. Xu, Y. Du, H. Chen, J. Chen, T. Ding, D. Sun, D. H. Kim, Z. Lin and X. Zhou, *Chem. Soc. Rev.*, 2024, **53**, 7202–7298.
7 Y. Matsuda, H. Nakashima, M. Morita and Y. Takasu, *J. Electrochem. Soc.*, 1981, **128**, 2552.
8 Z. Jian, W. Luo and X. Ji, *J. Am. Chem. Soc.*, 2015, **137**, 11566–11569.
9 C. Zhan, T. Wu, J. Lu and K. Amine, *Energy Environ. Sci.*, 2018, **11**, 243–257.
10 S. Komaba, T. Hasegawa, M. Dahbi and K. Kubota, *Electrochem. Commun.*, 2015, **60**, 172–175.
11 N. Naveen, S. C. Han, S. P. Singh, D. Ahn, K.-S. Sohn and M. Pyo, *J. Power Sources*, 2019, **430**, 137–144.
12 H. Chen, X.-W. Gao, Q. Li, R.-Z. Niu, S.-S. Wang, Q.-F. Gu, J.-J. Mu and W.-B. Luo, *J. Mater. Chem. A*, 2024, **12**, 6261–6268.
13 A. Eftekhari, *J. Power Sources*, 2004, **126**, 221–228.
14 X. Bie, K. Kubota, T. Hosaka, K. Chihara and S. Komaba, *J. Mater. Chem. A*, 2017, **5**, 4325–4330.
15 A. V, B. John and M. Td, *ACS Appl. Energy Mater.*, 2020, **3**, 9478–9492.
16 S. Chong, Y. Chen, Y. Zheng, Q. Tan, C. Shu, Y. Liu and Z. Guo, *J. Mater. Chem. A*, 2017, **5**, 22465–22471.
17 X. Wu, Z. Jian, Z. Li and X. Ji, *Electrochem. Commun.*, 2017, **77**, 54–57.
18 J. Liao, Q. Hu, Y. Yu, H. Wang, Z. Tang, Z. Wen and C. Chen, *J. Mater. Chem. A*, 2017, **5**, 19017–19024.
19 X. Ren, Q. Zhao, W. D. McCulloch and Y. Wu, *Nano Res.*, 2017, **10**, 1313–1321.
20 J. Ge, L. Fan, J. Wang, Q. Zhang, Z. Liu, E. Zhang, Q. Liu, X. Yu and B. Lu, *Adv. Energy Mater.*, 2018, **8**, 1801477.
21 B. Tian, W. Tang, K. Leng, Z. Chen, S. J. R. Tan, C. Peng, G.-H. Ning, W. Fu, C. Su, G. W. Zheng and K. P. Loh, *ACS Energy Lett.*, 2017, **2**, 1835–1840.
22 N. Naveen, W. B. Park, S. P. Singh, S. C. Han, D. Ahn, K.-S. Sohn and M. Pyo, *Small*, 2018, **14**, 1803495.
23 X. Song, S. N. Schneider, G. Cheng, J. F. Khoury, M. Jovanovic, N. Yao and L. M. Schoop, *Chem. Mater.*, 2021, **33**, 8070–8078.
24 C. F. van Bruggen, R. J. Haange, G. A. Wiegers and D. K. G. de Boer, *Physica B+C*, 1980, **99**, 166–172.
25 W. Li, N. Wolff, A. Kumar Samuel, Y. Wang, V. P. Georgiev, L. Kienle and A. Y. Ganin, *ChemElectroChem*, 2023, **10**, e202300428.
26 H. Euchner and A. Groß, *Phys. Rev. Mater.*, 2022, **6**, 040302.
27 M. Sotoudeh and A. Groß, *Curr. Opin. Electrochem.*, 2024, **46**, 101494.
28 J. Döhn and A. Groß, *Adv. Energy Sustainability Res.*, 2024, **5**, 2300204.
29 J. Sun, A. Ruzsinszky and J. P. Perdew, *Phys. Rev. Lett.*, 2015, **115**, 036402.
30 A. V. Krukau, O. A. Vydrov, A. F. Izmaylov and G. E. Scuseria, *J. Chem. Phys.*, 2006, **125**, 224106.
31 C. M. Fang, P. R. Tolsma, C. F. v. Bruggen, R. A. d. Groot, G. A. Wiegers and C. Haas, *J. Phys.: Condens. Matter*, 1996, **8**, 4381.
32 C. M. Fang, C. F. v. Bruggen, R. A. d. Groot, G. A. Wiegers and C. Haas, *J. Phys.: Condens. Matter*, 1997, **9**, 10173.
33 M. D. Johannes, K. Swider-Lyons and C. T. Love, *Solid State Ionics*, 2016, **286**, 83–89.
34 A. Chakraborty, M. Dixit, D. Aurbach and D. T. Major, *npj Comput. Mater.*, 2018, **4**, 60.
35 J. B. Goodenough and Y. Kim, *Chem. Mater.*, 2010, **22**, 587–603.
36 R. Hausbrand, G. Cherkashinin, H. Ehrenberg, M. Gröting, K. Albe, C. Hess and W. Jaegermann, *Mater. Sci. Eng. B*, 2015, **192**, 3–25.
37 S. J. Hibble, R. I. Walton and D. M. Pickup, *J. Chem. Soc., Dalton Trans.*, 1996, 2245–2251.
38 S. Kobayashi, N. Katayama, T. Manjo, H. Ueda, C. Michioka, J. Sugiyama, Y. Sassa, O. K. Forslund, M. Månsson, K. Yoshimura and H. Sawa, *Inorg. Chem.*, 2019, **58**, 14304–14315.
39 N. P. N. Puneeth, S. D. Kaushik and R. Kalai Selvan, *ACS Appl. Energy Mater.*, 2024, **7**, 2600–2613.
40 Y. Hironaka, K. Kubota and S. Komaba, *Chem. Commun.*, 2017, **53**, 3693–3696.
41 J.-Y. Hwang, J. Kim, T.-Y. Yu, S.-T. Myung and Y.-K. Sun, *Energy Environ. Sci.*, 2018, **11**, 2821–2827.
42 X. H. Rui, N. Ding, J. Liu, C. Li and C. H. Chen, *Electrochim. Acta*, 2010, **55**, 2384–2390.
43 Z. Wu, J. Zou, S. Chen, X. Niu, J. Liu and L. Wang, *J. Power Sources*, 2021, **484**, 229307.
44 Y. Lei, D. Han, J. Dong, L. Qin, X. Li, D. Zhai, B. Li, Y. Wu and F. Kang, *Energy Storage Mater.*, 2020, **24**, 319–328.
45 H. Wang, D. Zhai and F. Kang, *Energy Environ. Sci.*, 2020, **13**, 4583–4608.
46 P. K. Jha, S. K. Parate, K. Sada, K. Yoshii, T. Masese, P. Nukala, G. Sai Gautam, V. Pralong, M. Fichtner and P. Barpanda, *Small*, 2024, **20**, 2402204.

47 S. Zhao, Z. Liu, G. Xie, Z. Guo, S. Wang, J. Zhou, X. Xie, B. Sun, S. Guo and G. Wang, *Energy Environ. Sci.*, 2022, **15**, 3015–3023.
48 G. Suo, B. Zhao, R. Mu, C. Lin, S. Javed, X. Hou, X. Ye, Y. Yang and L. Zhang, *J. Energy Storage*, 2024, **77**, 109801.
49 B. Zhao, G. Suo, R. Mu, C. Lin, J. Li, X. Hou, X. Ye, Y. Yang and L. Zhang, *J. Colloid Interface Sci.*, 2024, **668**, 565–574.
50 Q. Tang, C. Liu, B. Zhang and W. Jie, *J. Solid State Chem.*, 2018, **262**, 53–57.
51 Y. Zhang, D. A. Kitchaev, J. Yang, T. Chen, S. T. Dacek, R. A. Sarmiento-Pérez, M. A. L. Marques, H. Peng, G. Ceder, J. P. Perdew and J. Sun, *npj Comput. Mater.*, 2018, **4**, 9.